

PAPER

## Development of a CMOS MEMS pressure sensor with a mechanical force-displacement transduction structure

To cite this article: Chao-Lin Cheng *et al* 2015 *J. Micromech. Microeng.* **25** 125024

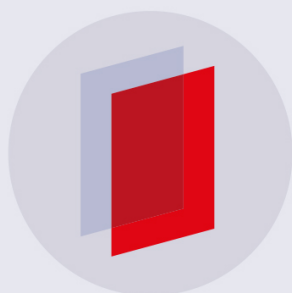
View the [article online](#) for updates and enhancements.

### Related content

- [Determining the thermal expansion coefficient of thin films for a CMOS MEMS process using test cantilevers](#)  
Chao-Lin Cheng, Ming-Han Tsai and Welleun Fang
- [Design and application of a metal wet-etching post-process for the improvement of CMOS-MEMS capacitive sensors](#)  
Ming-Han Tsai, Chih-Ming Sun, Yu-Chia Liu *et al.*
- [Monolithic integration of capacitive sensors using a double-side CMOS MEMS post process](#)  
Chih-Ming Sun, Chuanwei Wang, Ming-Han Tsai *et al.*

### Recent citations

- [Performance enhance of CMOS-MEMS thermoelectric infrared sensor by using sensing material and structure design](#)  
Ting-Wei Shen *et al*
- [Early-Warning System With Quasi-Distributed Fiber Optic Sensor Networks and Cloud Computing for Soil Slopes](#)  
Dong-Sheng Xu *et al*
- [MEMS capacitive pressure sensor monolithically integrated with CMOS readout circuit by using post CMOS processes](#)  
Munseon Jang and Kwang-Seok Yun



**IOP | ebooks™**

Bringing you innovative digital publishing with leading voices to create your essential collection of books in STEM research.

Start exploring the collection - download the first chapter of every title for free.

# Development of a CMOS MEMS pressure sensor with a mechanical force-displacement transduction structure

Chao-Lin Cheng<sup>1</sup>, Heng-Chung Chang<sup>1</sup>, Chun-I Chang<sup>2</sup>  
and Weileun Fang<sup>1,2</sup>

<sup>1</sup> Power Mechanical Engineering, National Tsing Hua University, Hsinchu, Taiwan

<sup>2</sup> Institute of NanoEngineering and MicroSystems, National Tsing Hua University, Hsinchu, Taiwan

E-mail: [fang@pme.nthu.edu.tw](mailto:fang@pme.nthu.edu.tw)

Received 15 July 2015, revised 12 September 2015

Accepted for publication 29 September 2015

Published 9 November 2015



## Abstract

This study presents a capacitive pressure sensor with a mechanical force-displacement transduction structure based on the commercially available standard CMOS process (the TSMC 0.18  $\mu\text{m}$  1P6M CMOS process). The pressure sensor has a deformable diaphragm to support a movable plate with an embedded sensing electrode. As the diaphragm is deformed by the ambient pressure, the movable plate and its embedded sensing electrode are displaced. Thus, the pressure is detected from the capacitance change between the movable and fixed electrodes. The undeformed movable electrode will increase the effective sensing area between the sensing electrodes, thereby improving the sensitivity. Experimental results show that the proposed pressure sensor with a force-displacement transducer will increase the sensitivity by 126% within the 20 kPa–300 kPa absolute pressure range. Moreover, this study extends the design to add pillars inside the pressure sensor to further increase its sensing area as well as sensitivity. A sensitivity improvement of 117% is also demonstrated for a pressure sensor with an enlarged sensing electrode (the overlap area is increased two fold).

Keywords: pressure sensor, force-displacement transduction structure, CMOS MEMS

(Some figures may appear in colour only in the online journal)

## 1. Introduction

Micro-electromechanical system (MEMS) pressure sensors have been extensively applied in consumer electronics, automotive systems, environmental monitoring, medical diagnostics, etc. Various fabrication approaches, such as surface micromachining and bulk micromachining have been reported to meet the requirements of related applications [1, 2]. To leverage existing foundry resources, the standard complementary metal oxide semiconductor (CMOS) processes have been exploited to fabricate MEMS devices [3, 4]. In this regard, the CMOS metal and dielectric films are not only employed as the electrical routing and isolation layers, but also exploited as suspended microstructures after the post-CMOS processing. Thus, the CMOS process technology enables the monolithic integration of MEMS structures and sensing circuits, and thus

could further reduce the packaging efforts and minimize the microsensors required. The footprint of sensing units is an important concern not only for cost but also for some applications. Moreover, the parasitic capacitance of capacitive-type sensors can be reduced after the integration of sensing circuits with MEMS devices using the CMOS MEMS process. To date, the CMOS MEMS process has been employed to implement various MEMS sensors, such as inertial sensors, magnetometers, and pressure sensors, etc. [3–6].

CMOS MEMS pressure sensors that have been implemented using available foundry processes have been reported in [7–9]. Existing CMOS MEMS pressure sensors mainly consist of a flexible diaphragm with an embedded deformable sensing electrode and a fixed reference sensing electrode. The diaphragm and sensing electrodes are formed by the metal and dielectric layers. As the diaphragm is deformed by the applied

pressure load, the gap between the deformable and fixed sensing electrodes is changed. The pressure is thus detected from the capacitance change. Many approaches have been reported for improving the sensitivity of capacitive microsensors, such as reducing the sensing gap [10], and increasing the dielectric constant [11]. However, limited designs are available for CMOS MEMS devices due to the fixed layers provided by the standard process. The concept of integrating a rigid electrode with a flexible mechanical structure for capacitive microsensors has been reported in [12–14]. The rigid sensing electrode and flexible diaphragm are linked by a mechanical support to form the force-displacement transduction structure. Thus, the deformation of the flexible membrane will be detected from the displacement of the rigid capacitive-sensing electrode.

This study exploits the concept in [14] to design a CMOS MEMS capacitive pressure sensor with a movable sensing electrode attached to a deformable diaphragm, as shown in figure 1(a). The sensitivity of the CMOS MEMS pressure sensor can be improved by the proposed parallel-plate gap-closing sensing electrodes. The existing design, with a deformable sensing electrode embedded in the flexible diaphragm, is also fabricated using the same process, as shown for comparison in figure 1(b). The devices are designed and implemented based on the Taiwan Semiconductor Manufacture Company (TSMC) 0.18  $\mu\text{m}$  1P6M CMOS process. The movable and deformable suspended mechanical structures, electrical routing, and sacrificial layer are thus implemented by using the stacking of metal and dielectric films fabricated by the CMOS process. An in-house post-CMOS etching process is required to release the MEMS structures. Moreover, the pressure sensor with a movable sensing electrode with a greater area than that of the diaphragm is also demonstrated to further enhance the sensing capacitance. Note that the present force-displacement transduction structure could be further applied to other CMOS MEMS sensors.

## 2. Sensor design and analysis

This study designs and implements a pressure sensor with a mechanical force-displacement transduction structure based on the TSMC 0.18  $\mu\text{m}$  1P6M CMOS process. In comparison, the existing pressure sensor design with deformable diaphragm and sensing electrode is also designed and implemented to prove the concept. Moreover, the proposed design concept using the standard CMOS process is further extended to add mechanical pillars on the pressure sensor to increase its sensitivity.

### 2.1. Sensor design—pressure sensor with force-displacement transducer

As illustrated in figure 1(a), the proposed sensor design (I) consists of a deformable diaphragm (to act as the force-displacement transduction structure), a mechanical support, a movable plate with embedded sensing electrode, and a fixed sensing electrode. The design is formed by the stacking of metal and dielectric layers as depicted by different colors in

figure 1(a). For instance, the sensing electrode embedded in movable plate is formed by the metal-3 (M3) layer, and the fixed sensing electrode is formed by the metal-1 (M1) layer. Note that the gap between the movable and fixed sensing electrodes is defined by the thickness of the sacrificed metal-2 (M2) layer. The symmetric layer stacking in [15] is exploited to design the movable plate with an embedded sensing electrode to reduce the deformations due to the residual stresses and CTE (coefficient of thermal expansion) mismatch of the thin films. Thus, the movable plate with the embedded sensing electrode consists of two metal layers (M3 and M4) and three dielectric layers (IMD2–4). The tungsten via array is distributed between two metal layers for the electrical routing of the movable sensing electrode.

This study is focused on absolute pressure sensor designs. Thus, the reference chamber indicated in figure 1 is sealed in a vacuum environment during the processes. The initial sensing capacitance is determined by the area of the sensing electrodes and the initial sensing gap defined by the M2 layer thickness. The diaphragm will be deformed by the ambient pressure and cause the displacement of the movable plate. Thus, the gap between the movable and fixed sensing electrodes is changed, and the pressure is then detected by the change in capacitance between the electrodes. Compared with the design in figure 1(b), the present sensor in figure 1(a) employs the undeformed movable electrode design to increase the effective sensing area between the sensing electrodes. As a result, the sensing capacitance is increased. Note that the two pressure sensors in figure 1 have the same diaphragm dimensions for fair comparison.

### 2.2. Sensor analysis

As indicated in figure 1(b) uniform pressure  $P$  is applied on the square diaphragm (edge length is  $2a$ , marked in figure 2(a)) with fully clamped edges. The diaphragm will be deformed due to the pressure difference between the reference vacuum chamber and ambient pressure  $P$ . The out-of-plane deflection  $z$  of the diaphragm at any position  $(x, y)$  (note that  $x = 0, y = 0$  denotes the center of square diaphragm) caused by pressure  $P$  can be expressed as [16],

$$z(x, y) = 0.0213P \left( \frac{a^4}{D} \right) \left( 1 - \frac{x^2}{a^2} \right)^2 \left( 1 - \frac{y^2}{a^2} \right)^2 \quad (1)$$

where  $D$  is the flexural rigidity of the diaphragm. The capacitance change after applying a uniform pressure can be expressed as [17],

$$\Delta C = C_{\text{deformation}} - C_0 = \varepsilon_0 \varepsilon_r \iint \frac{dx dy}{g_0 - z(x, y)} - \frac{\varepsilon_0 \varepsilon_r A}{g_0} \quad (2)$$

where  $\varepsilon_0$  is the permittivity of air,  $\varepsilon_r$  is the relative dielectric constant,  $A$  is overlap area of sensing electrodes, and  $g_0$  is the initial sensing gap. Thus, the sensitivity  $S$  of the capacitive pressure sensor becomes,

$$S = \left( \frac{\Delta z}{\Delta P} \times \frac{\Delta C}{\Delta z} \right) \times \left( \frac{\Delta V}{\Delta C} \right) = (S_{\text{mechanical}}) \times (S_{\text{electrical}}) \quad (3)$$

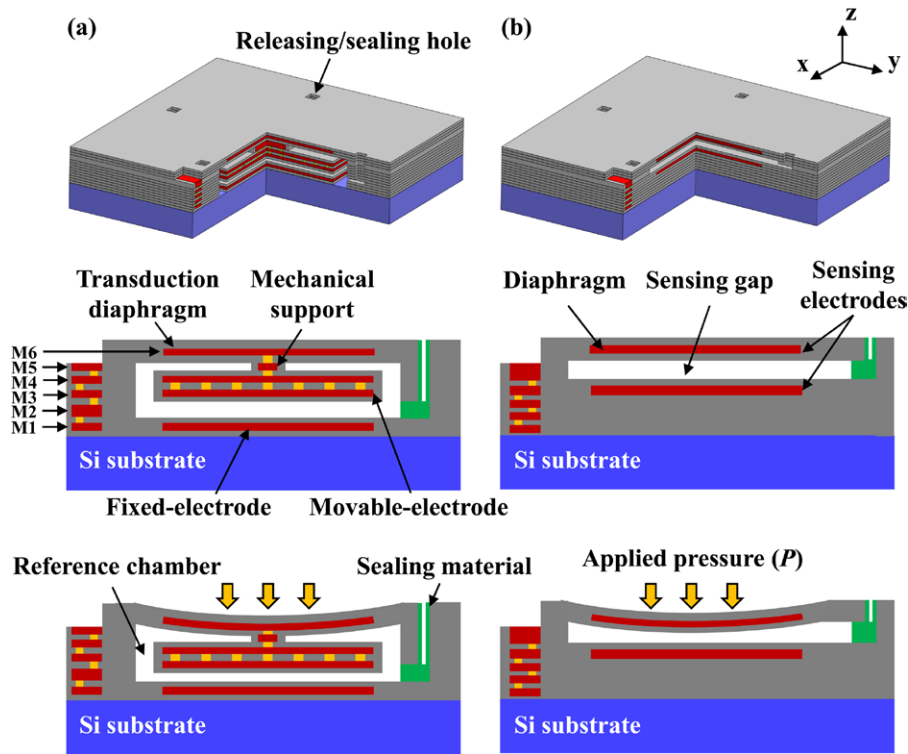


**Figure 1.** The design schematic of the presented pressure sensors. (a) Proposed design I (with force-displacement transduction structure). (b) The existing design (without transduction structure).

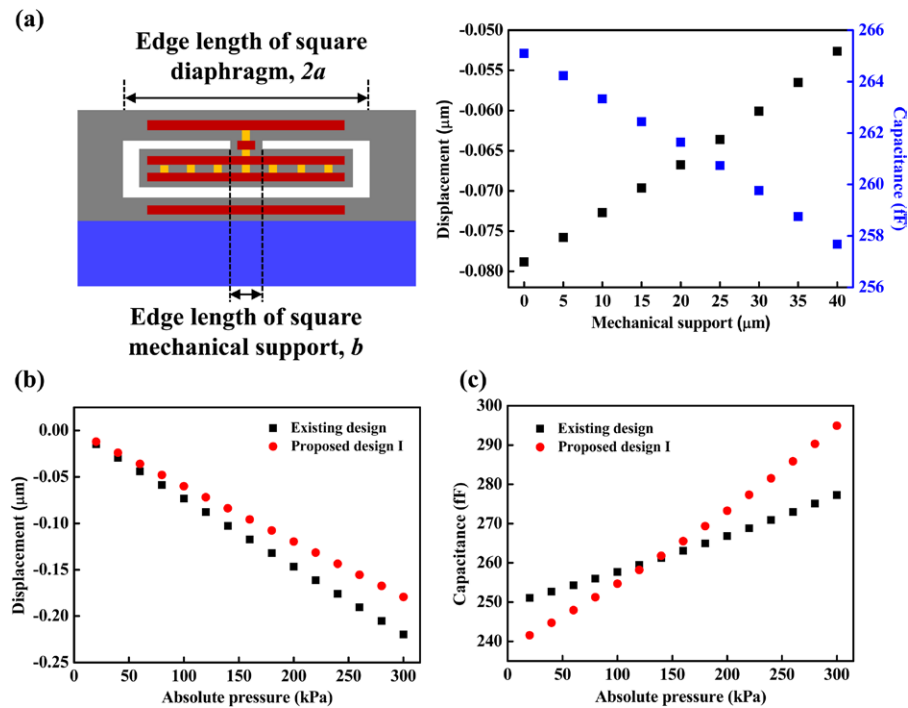


**Figure 2.** The pressure sensor performance predictions for (a) different sizes of mechanical support (from  $b = 0 \mu\text{m}$  to  $b = 40 \mu\text{m}$ ), and (b, c) comparison of proposed design I and the existing design.

where a pressure difference  $\Delta P$  causes diaphragm deflection  $\Delta z$  and the output capacitance  $\Delta C$  is then detected by the sensing electrodes. After that, a capacitance-to-voltage ( $C$ - $V$ ) circuit is employed to convert the output single  $\Delta C$  to voltage change  $\Delta V$ . The net capacitance change of the conventional

pressure sensor with a deformable sensing electrode shown in figure 1(b) is determined from the integration of equation (2). The net capacitance change of the proposed pressure sensor with undeformed sensing electrode shown in figure 1(a) can be simplified as,

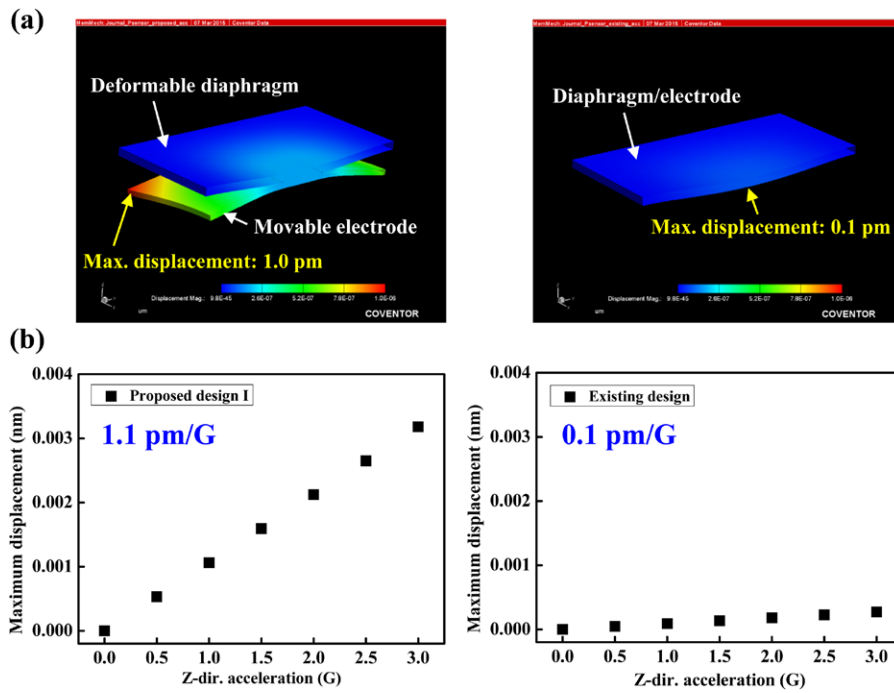


Figure 3. (a, b) Sensitivity to vibration noise evaluated by FEM simulations.

$$\Delta C = C_{\text{deformation}} - C_0 = \frac{\epsilon_0 \epsilon_r A \Delta z}{g_0^2 - g_0 \Delta z} \quad (4)$$

where  $A$  and  $\Delta z$  are respectively the area and displacement of the undeformed sensing electrode. Moreover,  $\Delta z$  can be determined by the diaphragm deflection at  $z(0, 0)$ .

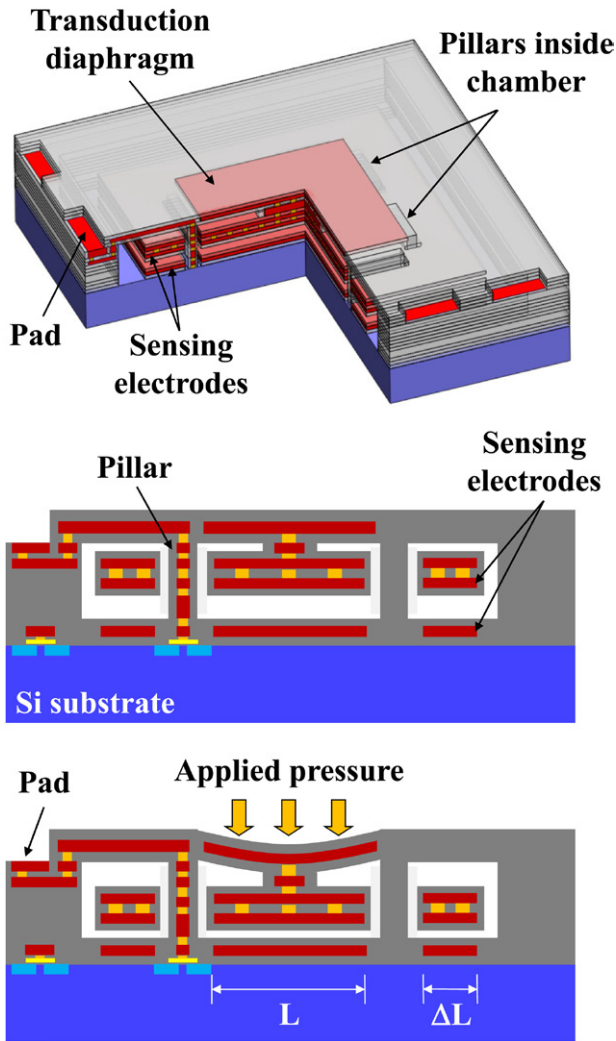
According to equations (1)–(3), the sensitivity of pressure sensor can be enhanced by varying the dimensions of diaphragm. However, the sensing range of the sensor will also be influenced. Moreover, the available metal and dielectric stacking layers are limited by the standard CMOS process. On the other hand, as indicated in equation (4), the output capacitance as well as the sensitivity of proposed pressure sensor design I can be improved by increasing the area of the sensing electrodes. This design alteration is not limited by the available CMOS films. The sensing range of the pressure sensor remains the same after the area of the sensing electrode is changed. Note that the diaphragm deformation will be influenced by the rigid central mechanical support for proposed pressure sensor design I in figure 1(a). As indicated in figure 2(a), the edge length of the square mechanical support is  $b$ . The simulation results in figure 2(a) further depict the central deformations of square diaphragm ( $2a = 160 \mu\text{m}$ ) with mechanical supports of different size ( $b = 0\text{--}40 \mu\text{m}$ ) at  $P = 101 \text{ kPa}$ . The results indicate that the central deformation of the diaphragm and  $\Delta z$  decrease by 33% as the size of mechanical support increases from  $b = 0 \mu\text{m}$  to  $b = 40 \mu\text{m}$ . Due to post-CMOS process considerations, the  $b = 30 \mu\text{m}$  mechanical support is chosen in this study. According to these design parameters, figures 2(b) and (c) show the sensor performances predicted by finite element method (FEM) simulations. The simulations in figure 2(b) indicate that proposed design I with a mechanical support has a smaller central deflection of diaphragm. Thus, the initial capacitance of proposed design I is

Table 1. The specifications of CMOS MEMS pressure sensors with (proposed design I) and without (existing design) force-displacement transduction structure.

Items	Existing design	Proposed design I	Unit
Transduction diaphragm size	$160 \times 160 \times 5.2$		$\mu\text{m}^3$
Electrode size	$150 \times 150$		$\mu\text{m}^2$
Absolute pressure range	20–300		kPa
Designed initial capacitance ( $2 \times 2$ array)	1.03	1.02	pF
Sensitivity	0.19	0.43	fF kPa $^{-1}$
Nonlinearity	2.2	4.7	%
TCO	−0.04	−0.07	% °C $^{-1}$
TCS	−0.32	−0.43	% °C $^{-1}$

smaller than that of the existing design, as predicted in figure 2(c). These results also indicate that the sensitivity of proposed design I has been increased to  $0.19 \text{ fF kPa}^{-1}$  ( $0.09 \text{ fF kPa}^{-1}$  for the existing design in figure 1(b)) within the 20 kPa–300 kPa pressure range. Thus, despite of the smaller initial capacitance, the sensitivity of proposed design I still has a 2.11-fold improvement in sensitivity. Note that the pressure sensor array can also be employed to increase the capacitance sensing signal. In applications, a pressure sensor consisting of  $2 \times 2$  sensing components has been implemented for demonstration. Detailed design specifications of the two pressure sensors are listed in table 1.

The FEM simulations in figure 3 evaluate the noise caused by vibration on the sensors. The simulation results in figure 3(a) predict the deformations of the deformable diaphragm and movable plate (only for proposed design I) as both sensors are under acceleration in the out-of-plane ( $z$  direction in figure 1). The simulation results in figure 3(b) further



**Figure 4.** The design schematic of proposed design II further extends the concept in figure 1(a) to add pillars inside the pressure sensor to increase the area of the sensing electrodes.

predict the maximum deflection of the sensors in figure 3(a) as the acceleration is increased from 0 G to 3 G. The sensor of proposed design I has an additional plate attached to the deformable diaphragm. Therefore, the movable electrode on proposed design I has a larger displacement under the same acceleration. According to the predicted results in figure 3(b), the pressure sensors have the displacements of  $1.1 \text{ pm G}^{-1}$  (for proposed design I) and  $0.1 \text{ pm G}^{-1}$  (for the existing design). Note that these values are two orders of magnitude lower than the minimum detectable signal. Thus, the noise caused by the acceleration can be ignored.

### 2.3. Extension of the sensor design—adjustable sensing area

The concept in figure 1(a) (proposed design I) can be further extended by adding pillars inside the pressure sensor to support the transduction diaphragm by using the same fabrication processes, as shown in figure 4. In this design (proposed design II), the planar dimension of the movable plate and the embedded sensing electrode is allowed to be larger than that

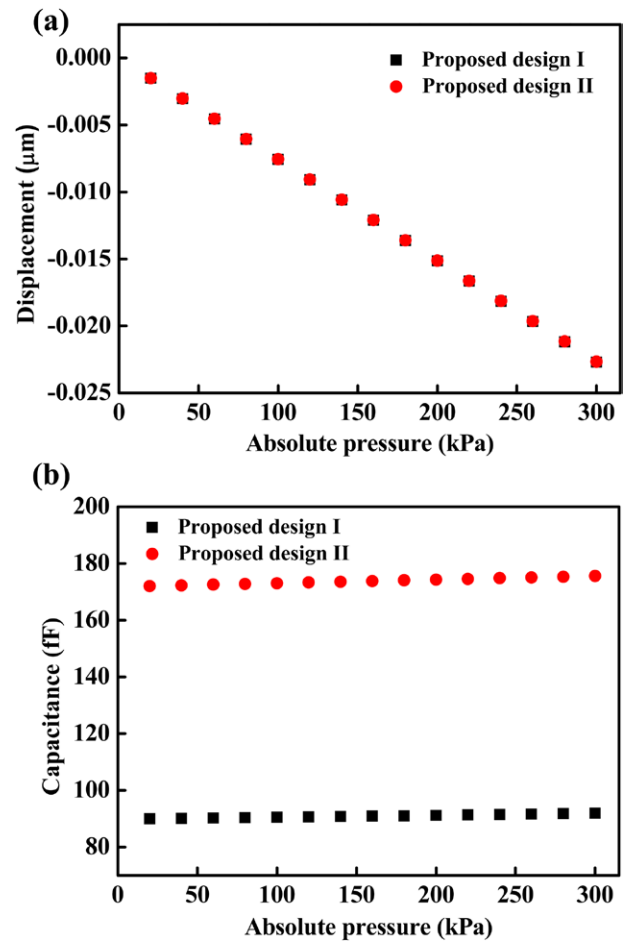


**Figure 5.** The performance prediction for pressure sensors (proposed designs I and II) for (a) center displacement, and (b) output capacitance for adjustable sensing area comparison.

of the deformable diaphragm. Thus the area of the sensing electrodes can be greater, and the sensitivity of sensor can be further improved as mentioned in equation (4). As indicated in figure 4, the deformable transduction diaphragm is supported by the pillars. The planar dimension of the deformable diaphragm is also defined by the pillars. Moreover, the openings on the movable plate are designed to allow the pillars to anchor on the substrate. In this regard, the area of the movable plate and the sensing electrodes are no longer limited by the planar dimension of the deformable diaphragm, and can be adjusted to meet the design requirement.

The FEM simulation results in figure 5 show the characteristics of two proposed sensor designs (proposed design I and proposed design II). These two designs have the same size of deformable diaphragm ( $100 \mu\text{m} \times 100 \mu\text{m}$ ), yet the sizes of movable plate and sensing electrodes are different. The movable plates with embedded sensing electrode are  $90 \mu\text{m} \times 90 \mu\text{m}$  (for proposed design I) and  $145 \mu\text{m} \times 145 \mu\text{m}$  (for proposed design II). Note that the movable plate of proposed design II has eight openings for the eight pillar supports ( $38 \mu\text{m} \times 16 \mu\text{m}$ ), and thus the net area of the sensing electrode is reduced. Nevertheless, proposed design II has increased the sensing area two fold. The simulation results in figure 5(a) indicate that proposed designs I and II have the same diaphragm

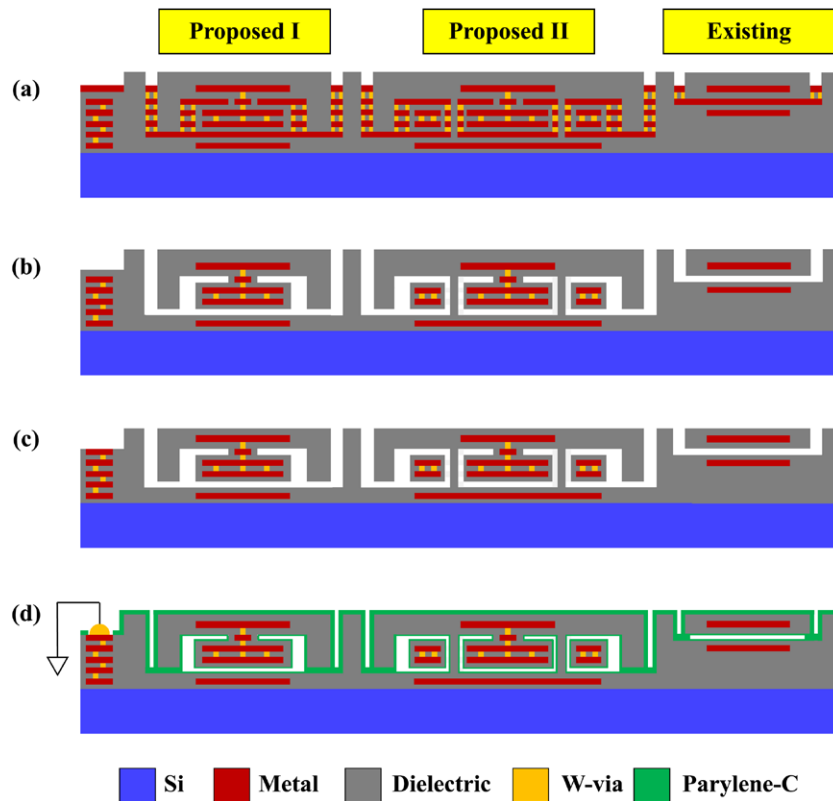


**Figure 6.** The steps of the fabrication process. (a) Chips are fabricated by the TSMC 0.18  $\mu\text{m}$  1P6M CMOS process. (b) Metal wet etching is used to define the movable plate, sensing gap, and pillar supports. (c) RIE exposes the wire bonding pad. (d) A 1  $\mu\text{m}$  thick Parylene-C coating seals the chamber and the chip is wire bonded on a PCB for testing.

deformation under the pressure loads. However, as illustrated in figure 5(b), the initial sensing capacitance (under 101 kPa) of the sensors can be increased from 91 fF to 173 fF by proposed design II. Moreover, the sensitivity can be increased by a further 81% within the sensing range of 20 kPa–300 kPa absolute pressure by proposed design II with sensing electrodes of greater area.

### 3. Fabrication and results

The steps in the fabrication process to implement the proposed and existing pressure sensor designs are shown in figure 6. Figure 6(a) depicts the stacking and patterning of metal and dielectric layers after the standard 0.18  $\mu\text{m}$  1P6M CMOS processes prepared by the TSMC. After that, the etching solution (which includes  $\text{H}_2\text{SO}_4$  and  $\text{H}_2\text{O}_2$ ) was employed to etch metal layers and tungsten via [18]. As illustrated in figure 6(b), the movable plate, sub-micron sensing gap, and pillar supports of the pressure sensor were defined in this process. The metal films for the sensing electrodes and electrical routings were protected by the dielectric films during the metal wet etching. Moreover, the movable plate with embedded sensing electrodes was suspended, and the sensing gap between electrodes was 0.53  $\mu\text{m}$  (determined by the M2 sacrificial layer). For the existing design, the sensing gap determined by the sacrificial metal layer M5 was also 0.53  $\mu\text{m}$ . As indicated in figure 6(c), reactive ion etching (RIE) was used to open the pads for wire

bonding. In addition, the thickness of the deformable diaphragm was also defined after the RIE etching. As shown in figure 6(d), the reference chamber of the pressure sensor was sealed by 1  $\mu\text{m}$  Parylene-C conformal coating for sensor measurement of absolute pressure. Note that the vacuum chamber for Parylene-C conformal coating process was near 10 Pa. Thus, the reference chamber of the presented pressure sensor after sealing by Parylene-C was also near 10 Pa. The chamber could also be sealed by other materials such as PECVD oxide, sputtering metal, etc. Finally the test chip was wire bonded on a printed circuit board (PCB) for the following characterizations and tests.

Figure 7 shows the typical fabrication results of the proposed and existing pressure sensor designs. The scanning electron microscopy (SEM) micrograph in figure 7(a) shows the fabricated chip containing the proposed and existing designs. As marked by the dashed lines, in this study the integration of  $2 \times 2$  sensor array design is employed to form a sensing unit to increase the capacitance sensing signal. The top left and right sensing units are used to compare the performances between proposed design I and the existing design. To make a fair comparison, these two different designs have the same diaphragm dimensions (160  $\mu\text{m} \times 160 \mu\text{m}$ ) and sensing gap. Moreover, the bottom right and left sensing units are used to compare the performances between proposed designs I and II. These two different designs also have the same diaphragm dimensions (100  $\mu\text{m} \times 100 \mu\text{m}$ ) and sensing gap. The SEM micrographs in figure 7(b) display the

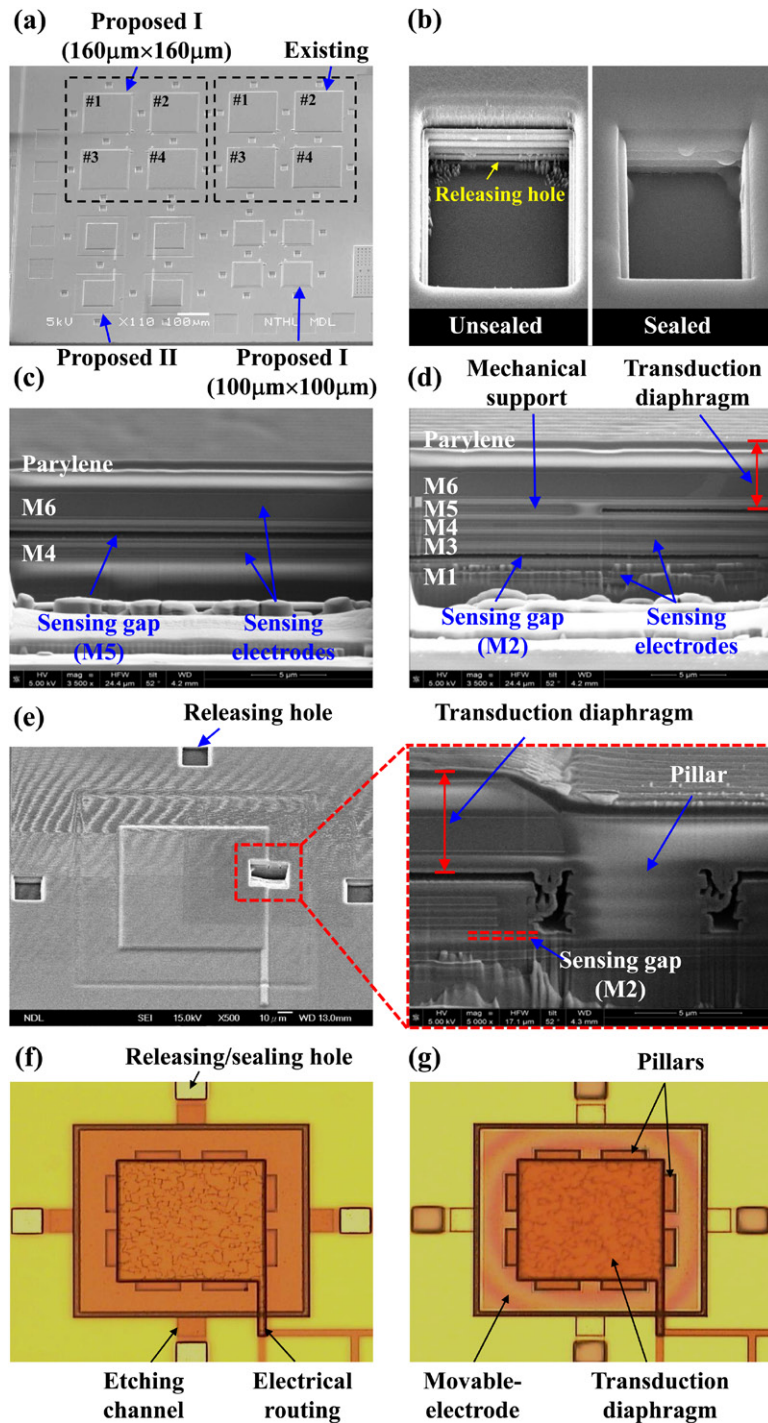


**Figure 7.** Fabrication results. (a) The fabricated chip containing the proposed and existing designs (the integration of  $2 \times 2$  sensor array as marked by the dash line). (b) The  $1 \mu\text{m}$  Parylene-C conformal coating on the releasing hole. FIB cross-section views of (c) the existing design, (d) proposed design I, (e) proposed design II. Micrographs of (f) chip prototype (figure 6(a)), and (g) structure releasing (figure 6(b)) of proposed design II.

releasing hole before and after conformal coating with the  $1 \mu\text{m}$  Parylene-C. The focused ion beam (FIB) cross-sections in figures 7(c) and (d) respectively show the layer stacking of the existing design and proposed design I. In figure 7(c), the deformable diaphragm with an embedded sensing electrode (M6 layer) and the fixed sensing electrode (M4 layer) for the existing design are observed. Figure 7(d) displays the key components inside the chamber of proposed design I,

and the deformable transduction diaphragm, mechanical support, and movable plate with embedded sensing electrodes are observed. The stacking of metal and dielectric layers in these structures is also observed. Moreover, the FIB cross-section in figure 7(e) shows the deformable transduction diaphragm and pillar inside the reference chamber of proposed design II. The micrographs in figures 7(f) and (g) show the fabricated chip of proposed design II before and after metal wet etching.

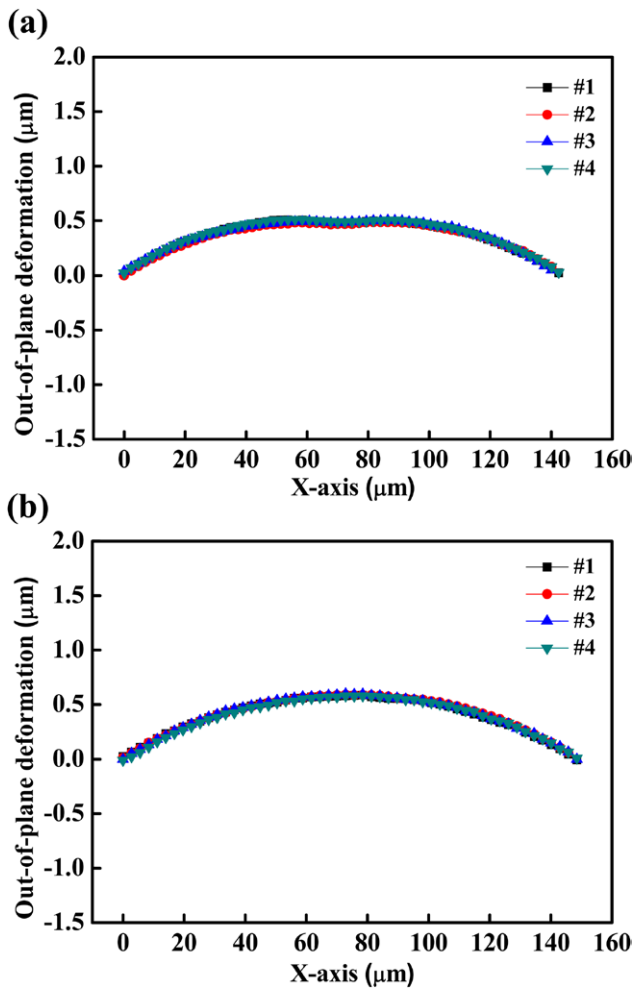


**Figure 8.** Surface profile of  $2 \times 2$  diaphragm array measured by optical interferometer to compare (a) proposed design I and (b) the existing design. Each four profiles (#1–#4) are associated with those shown in figure 7(a).

The deformable transduction diaphragm is supported by eight rectangular pillars. The movable plate inside the transparent dielectric cover is observed after the metal wet etching. It also indicates that the planar size of the movable plate and electrode is larger than the transduction diaphragm.

#### 4. Results and discussions

The proposed pressure sensors have been characterized and measured for proof of concept. The measurements will focus on proposed design I and the comparison of its performance with that of the existing design, as marked by the dashed lines in figure 7(a). The sensitivity improvement with proposed design II will also be further evaluated using the measurements.

##### 4.1. Initial deformation of the deformable transduction diaphragm

Due to the residual stresses of metal and dielectric films, the suspended deformable diaphragm has an initial deformation after the process. The surface profile of the pressure sensors

(such as the top surface of the deformable diaphragm indicated in the cross-sections of figure 1) were measured using an optical interferometer. The measurements in figure 8 show the initial deformation of the deformable diaphragms for proposed design I and the existing design after the process. The measurements were performed at an atmospheric pressure of 101 kPa. The four profiles (#1–#4) are characterized from the four sensors ( $2 \times 2$  sensors array) indicated in figure 7(a). The results show that the initial deformation of the deformable diaphragm has good uniformity for the fabricated sensors. The deformable diaphragms (with the planar dimensions of  $160 \mu\text{m} \times 160 \mu\text{m}$ ) for both designs are slightly bent upwards (with central deformation of near  $0.6 \mu\text{m}$ ). As mentioned in section 3, the reference chamber of the pressure sensor was near 10 Pa after vacuum sealing. Thus, the upward bending of the diaphragm is due to the residual stresses of the thin films. The results also indicate that the initial diaphragm deformations of the proposed and existing designs are similar. However, the center of the diaphragm of proposed design I has a slight concave deformation due to the existence of the stiff mechanical support.

##### 4.2. Sensitivity and linearity tests

Figure 9(a) illustrates the setup for pressure load testing. The test chip was wire bonded on a PCB, and placed inside the vacuum chamber for performance characterization. To demonstrate the present concept, this study characterized the pressure sensors of proposed design I and the existing design, as marked by the dash lines in figure 7(a). During the test, a pressure controller (GE, PACE5000) was used to specify and monitor the pressure of the vacuum chamber. The output capacitance change of the pressure sensors was measured by a commercial LCR meter (Agilent, 4980A). Measurements in figures 9(b) and (c) show output capacitance change from the sensors versus the absolute pressure of the test chamber. The full-scale measurement range is 20 kPa–300 kPa for absolute pressure. Figure 9(b) depicts the signals characterized from the sensors (proposed design I) before and after vacuum sealing by Parylene-C. The output capacitance did not change with pressure load for chips not sealed by Parylene-C (as indicated in figure 6(c)). For chips sealed by Parylene-C (as indicated in figure 6(d)), the output capacitance increases as the ambient pressure increases. In short, as the ambient pressure is increased, the bending (downward) of the deformable diaphragm is increased and further leads to decreasing of the sensing gap. The results show that the reference chamber of the pressure sensor is properly sealed by the Parylene-C coating. Measurements in figure 9(c) show that proposed design I has a sensitivity of  $0.43 \text{ fF kPa}^{-1}$  and non-linearity of 4.7% within the 20 kPa–300 kPa sensing range. In comparison, the existing design has a sensitivity of  $0.19 \text{ fF kPa}^{-1}$  and non-linearity of 2.2% within the same sensing range. This indicates that proposed design I could increase the sensitivity by 126% within the 20 kPa–300 kPa sensing range. Due to the initial deflection of the flexible diaphragm as indicated in figure 8, the sensitivities of for both designs are lower than the predicted results in figure 2(c). If the initial deformation

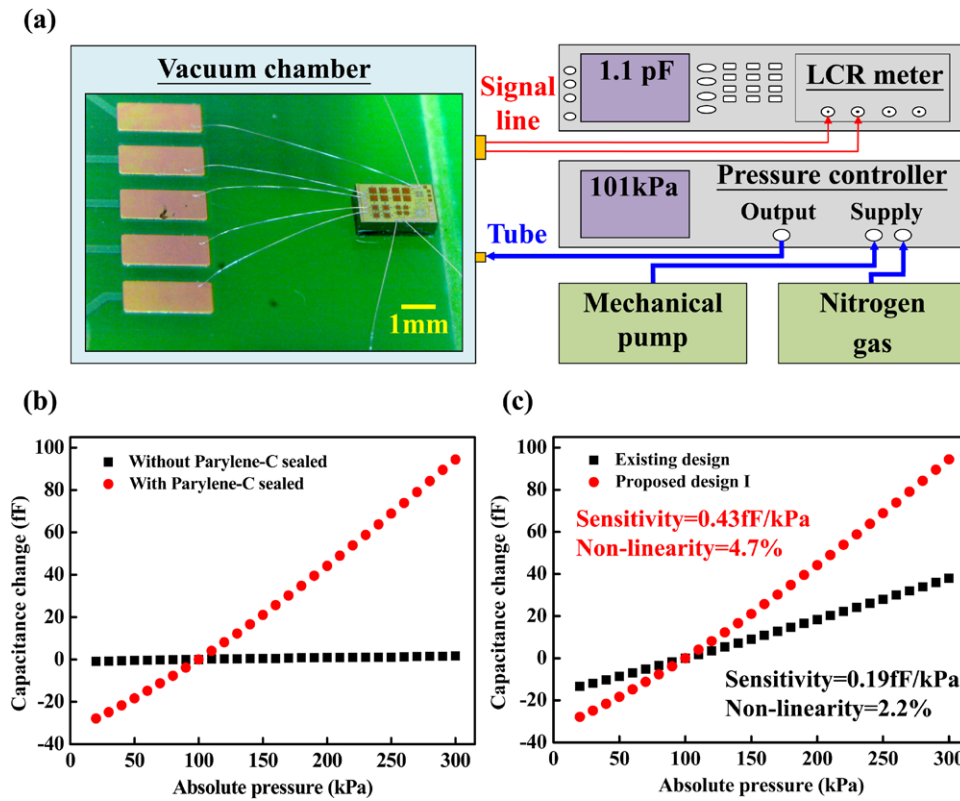


**Figure 9.** (a) The measurement setup to characterize the performance of pressure sensors. (b) Output capacitance before and after 1  $\mu\text{m}$  Parylene-C sealing. (c) Measured output capacitance change from the sensors versus pressure change (increments of 10 kPa) within the 20 kPa–300 kPa pressure range.

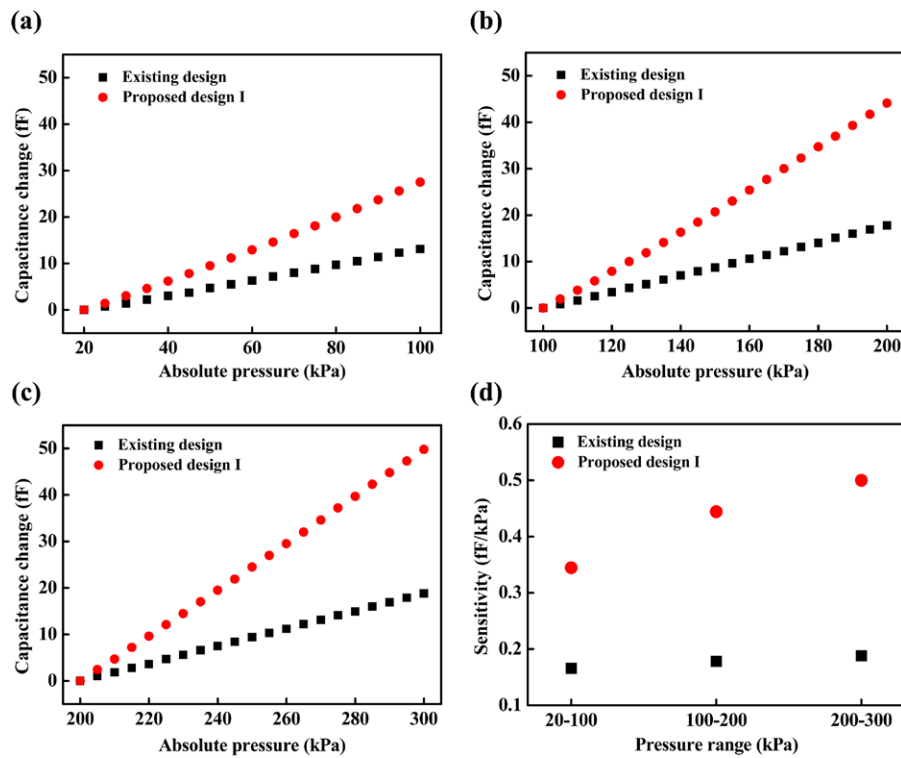


**Figure 10.** (a)–(c) Measured output capacitance change from sensors versus pressure change (increment 5 kPa) in three different pressure ranges (20 kPa–100 kPa, 100 kPa–200 kPa, and 200 kPa–300 kPa). (d) Sensitivity in these three different pressure ranges.

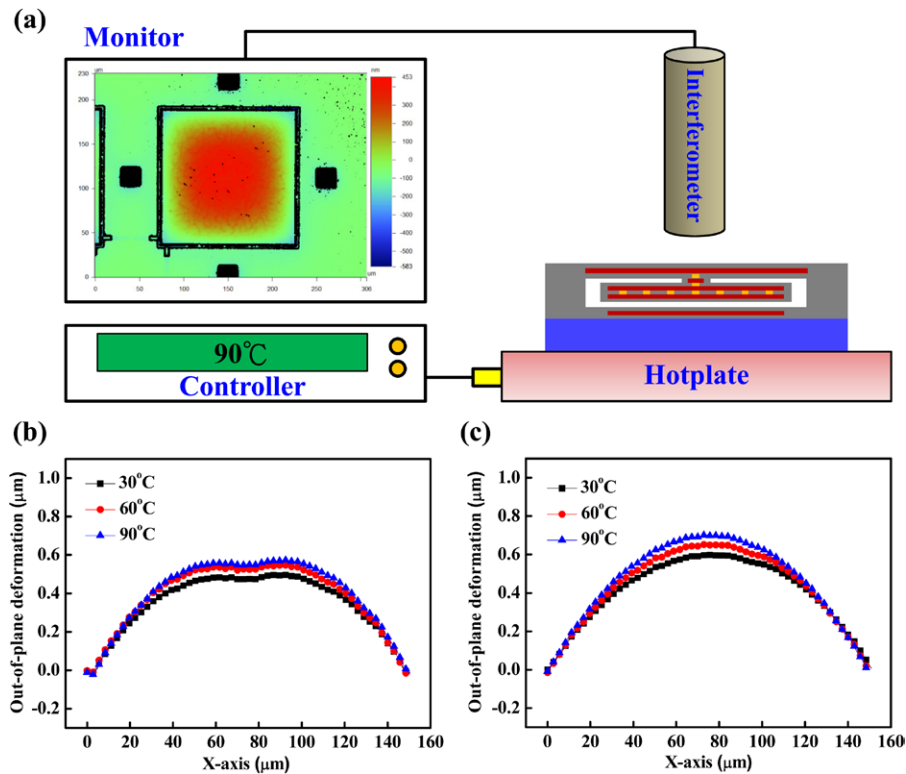


**Figure 11.** Characterization of diaphragm deflection at different temperatures. (a) Measurement setup. (b) Results for proposed design I. (c) Results for the existing design.

of diaphragm in figure 8 is considered, the predicted sensitivities of proposed design I and the existing design become  $0.32 \text{ fF kPa}^{-1}$  and  $0.17 \text{ fF kPa}^{-1}$ , respectively.

Measurements in figure 10 further investigate the variation of sensitivity at different pressure ranges for proposed design I and the existing design. Figures 10(a)–(c) show the variation of sensing capacitance with small pressure increments of 5 kPa at three different absolute pressure sensing ranges (20 kPa–100 kPa, 100 kPa–200 kPa, 200 kPa–300 kPa). The results show that the sensitivity of proposed design I increased from  $0.34 \text{ fF kPa}^{-1}$  to  $0.50 \text{ fF kPa}^{-1}$  as the absolute pressure sensing range changed from 20 kPa–100 kPa to 200 kPa–300 kPa. The non-linearity within these sensing ranges is 0.7–2.2%. The sensitivity of the existing design increased from  $0.16 \text{ fF kPa}^{-1}$  to  $0.19 \text{ fF kPa}^{-1}$  as the absolute pressure sensing range changed from 20 kPa–100 kPa to 200 kPa–300 kPa. The non-linearity within these sensing ranges is 0.7–1.9%. Figure 10(d) summarizes the sensitivity variation of the three different absolute pressure sensing ranges. The results indicate that the parallel-plate gap-closing sensing mechanism of proposed design I could significantly increase the sensitivity, especially in the high-pressure sensing range.

#### 4.3. Temperature sensitivity tests

Due to the CTE mismatch of metal and dielectric films, the temperature variation will introduce thermal stress to deflect the deformable diaphragm. To evaluate the thermal sensitivity of the present sensor with stacking of multilayer metal and dielectric films [19], this study also characterizes the pressure

sensors of proposed design I and the existing design at different ambient temperatures. Figure 11(a) shows the testing setup to measure the thermal deflection of the deformable diaphragm at different temperatures. The heating temperature of the test chip was specified by a commercial hot plate (Linkam Ltd, THMS600). Thermal deformation was measured by a commercial optical interferometer (Veeco Inc., NT-1100). The test chip was placed on the heating stage for long enough to reach the steady-state temperature before measurement. The results in figure 11(b) show the deflection profiles of proposed design I measured at three different temperatures (30 °C, 60 °C and 90 °C). The center displacement of the diaphragm (bent upward) is  $0.07 \mu\text{m}$  (from  $0.48 \mu\text{m}$  to  $0.55 \mu\text{m}$ ) as temperature increased from 30 °C to 90 °C. Thus, the thermal deformation of the diaphragm will increase the sensing gap and thus decrease the sensing capacitance. In comparison, as indicated in figure 11(c), the center displacement of the diaphragm (also bent upward) for the existing design is  $0.12 \mu\text{m}$  (from  $0.58 \mu\text{m}$  to  $0.70 \mu\text{m}$ ) for the same temperature elevation. Note that due to the existence of the stiff mechanical support, proposed design I has a smaller thermal deflection.

The sensing capacitances in figure 12 are measured from the pressure sensors (proposed design I and existing design) under various ambient pressures (20 kPa–300 kPa) and temperatures (30 °C, 60 °C and 90 °C). According to the measurements at 101 kPa, the temperature coefficient of offset (TCO) of proposed design I and the existing design are respectively  $-0.07\% \text{ } ^\circ\text{C}^{-1}$  and  $-0.04\% \text{ } ^\circ\text{C}^{-1}$  as temperature is elevated from 30 °C to 90 °C. The temperature coefficient of sensitivity (TCS) of proposed design I and the existing design

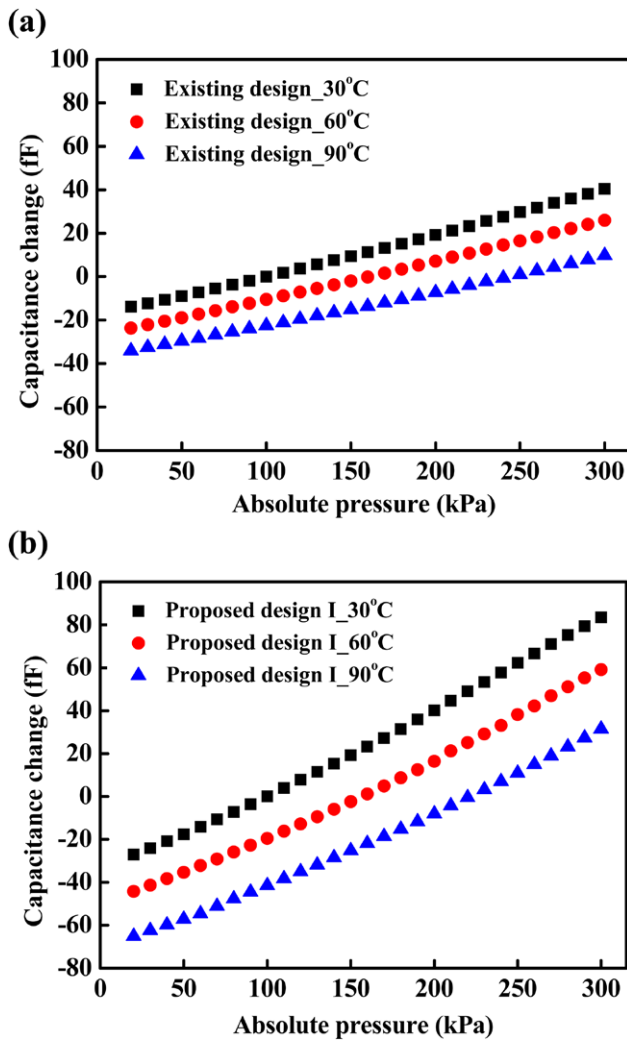


**Figure 12.** (a, b) Measurements of sensing capacitance under various pressures (20 kPa–300 kPa) and temperatures (30 °C, 60 °C and 90 °C).

are  $-0.43\% \text{ } ^\circ\text{C}^{-1}$  and  $-0.32\% \text{ } ^\circ\text{C}^{-1}$  respectively as temperature is elevated from 30 °C to 90 °C. Note that the diaphragm is bent upward due to the thermal deformation, as shown in figures 11(b) and (c). The sensing capacitance is decreased when temperature is increased, and thus the TCO and TCS are negative. The characteristics of the pressure sensors, including proposed design I and the existing design, are summarized in table 1.

**4.4. Performance evaluation of the sensor with adjustable sensing area design**

This study further characterized the pressure sensor of proposed design II with supporting pillars (as illustrated in figure 4), and also compared its performances with proposed design I. For fair comparison, the size of deformable diaphragms for design I and design II are the same ( $100 \mu\text{m} \times 100 \mu\text{m}$ ) in this demonstration. However, the overlap sensing area of proposed design II is two-fold higher than that of proposed design I. The measurement results in figure 13(a) show the

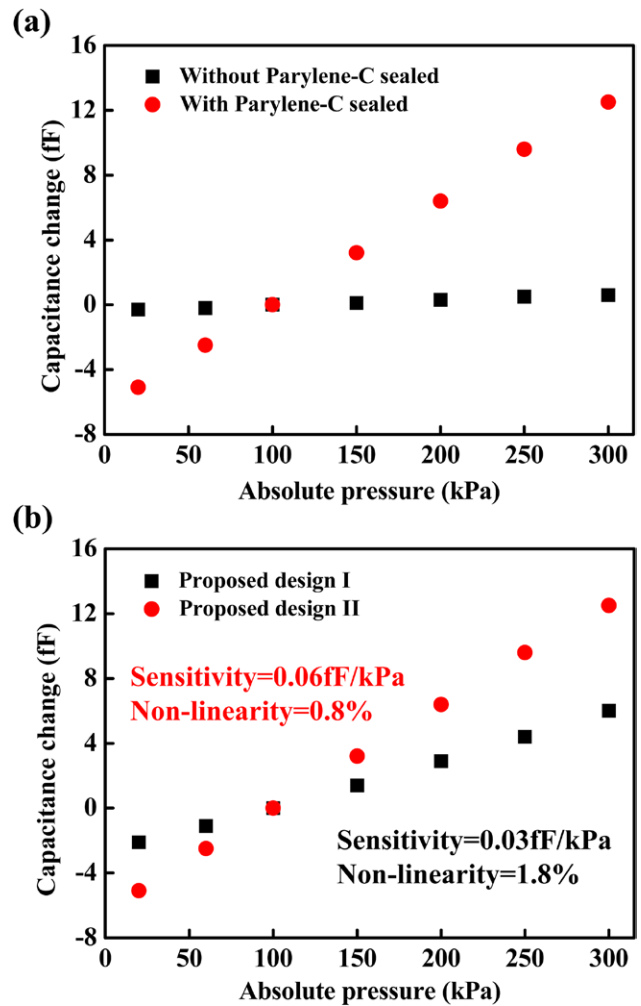


**Figure 13.** (a) Compared output signal from the sensor before and after Parylene-C sealing. (b) Measured output capacitance change from the sensors versus pressure change (increments of 50 kPa) within the 20 kPa–300 kPa pressure range.

output signals from the sensors before and after Parylene-C sealing. The results indicate that the reference chamber of the absolute pressure sensor has been successfully sealed by  $1 \mu\text{m}$  Parylene-C. Thus the diaphragm deformation and the sensing capacitance change are introduced by the ambient pressure change. Measurements in figure 13(b) indicate that proposed pressure sensor design II could improve the sensitivity by 117% (from  $0.03 \text{ fF kPa}^{-1}$  to  $0.06 \text{ fF kPa}^{-1}$ ) within the range of 20 kPa–300 kPa. This improvement in sensitivity is higher than predicted. The deviation is mainly due to the boundary conditions of the deformable diaphragm. The deformable diaphragm is supported by eight pillars inside the reference chamber, as indicated in figure 4. Compared with the perfect clamped edges, the pillars are not rigid enough and may cause an additional displacement of the sensing electrode. As a result, the measured capacitance output is larger than that predicted from simulation. In short, proposed design II could enlarge the area of the sensing electrode and further improve the sensitivity of the pressure sensor despite the sensing range of the sensor remaining unchanged.

## 5. Conclusions

In this study, a capacitive CMOS MEMS pressure sensor with a mechanical force-displacement transduction structure has been designed and implemented using the TSMC 0.18  $\mu\text{m}$  1P6M CMOS process. The effective sensing area has been increased by the undeformed movable plate with an embedded sensing electrode. Measurements indicate that the sensitivity of the pressure sensor with a mechanical force-displacement transduction structure (proposed design I) is improved by 126% within the sensing range of 20 kPa–300 kPa, as compared with the existing design. This study also characterized temperature sensitivities for proposed design I and the existing design, such as thermal deformation, the temperature coefficient of offset (TCO), and the temperature coefficient of sensitivity (TCS). Detailed measurement results are summarized in table 1. Moreover, supporting pillars are further designed and implemented in pressure sensor design II. For this pressure sensor with supporting pillars, the planar dimensions of the movable plate and the embedded sensing electrode are allowed to be larger than that of the deformable diaphragm. Thus, the sensitivity of the pressure sensor can be further improved. The sensitivity of proposed design II with sensing electrodes of larger area (overlap area increased two fold) is found to be improved by 117% within the sensing range of 20 kPa–300 kPa. Note that the size/shape of the movable plate and sensing electrodes can be further adjusted to meet the design requirement yet the sensing range (or the dimensions of the deformable diaphragm) remains the same. The applications of the force-displacement transduction structure presented in this study can be further employed to realize a fully differential sensing mechanism.

## Acknowledgments

This research was sponsored in part by the Ministry of Science and Technology of Taiwan under grants MOST-102-2221-E-007-027-MY3 and MOST-104-2622-E-007-003. The authors wish to thank the TSMC and the National Chip Implementation Center (CIC), Taiwan, for supporting the CMOS chip manufacturing. The authors would like to thank Sensirion AG for the technical and financial support. The authors would like to thank the National Center for High-Performance Computing (NCHC) for simulation tools. The authors would also like to thank the Center for Nanotechnology, Materials Science and Microsystems (CNMM) of the National Tsing Hua University and the National Nano Device Laboratory (NDL), Taiwan, for providing the process tool.

## References

- [1] Eaton W and Smith J 1997 Micromachined pressure sensors: review and recent developments *Smart Mater. Struct.* **6** 530–9
- [2] Pedersen T, Fragiaco G, Hansen O and Thomsen E 2009 Highly sensitive micromachined capacitive pressure sensor with reduced hysteresis and low parasitic capacitance *Sensors Actuators A* **154** 35–41
- [3] Fedder G 2005 CMOS-based sensors *Proc. IEEE Sensors Conf. (Irvine, CA, October 2005)* pp 125–8
- [4] Fang W, Li S-S, Cheng C-L, Chang C-I, Chen W-C, Liu Y-C, Tsai M-H and Sun C 2013 CMOS MEMS: a key technology towards the ‘More than Moore’ era *Proc. Transducers Conf. (Barcelona, Spain, June 2013)* pp 2513–8
- [5] Lakdawala H and Fedder G 2004 Temperature stabilization of CMOS capacitive accelerometers *J. Micromech. Microeng.* **14** 559–66
- [6] Chang C-I, Tsai M-H, Sun C-M and Fang W 2014 Development of CMOS-MEMS in-plane magnetic coils for application as a three-axis resonant magnetic sensor *J. Micromech. Microeng.* **24** 035016
- [7] Sun C-M, Wang C, Tsai M-H, Hsieh H-S and Fang W 2009 Monolithic integration of capacitive sensors using a double-side CMOS MEMS post process *J. Micromech. Microeng.* **19** 015023
- [8] Narducci N, Liu Y-C, Fang W and Tsai J 2013 CMOS MEMS capacitive absolute pressure sensor *J. Micromech. Microeng.* **23** 055007
- [9] Fujimori T, Takano H, Machida S and Goto Y 2009 Tiny ( $0.72\text{ mm}^2$ ) pressure sensor integrating MEMS and CMOS LSI with back-end-of-line MEMS platform *Proc. Transducers Conf. (Denver, CO, June 2009)* pp 1924–7
- [10] Reuter D, Bertz A, Billep D, Scheibner D, Buschnakowski S, Dotzel W and Gessner T 2005 In-process gap reduction of capacitive transducers *Proc. Transducers Conf. (Seoul, Korea, June 2005)* pp 1358–61
- [11] Kwon D, Lee T-I, Kim M S, Kim S, Kim T-S and Park I 2015 Porous dielectric elastomer based ultra-sensitive capacitive pressure sensor and its application to wearable sensing device *Proc. Transducers Conf. (Anchorage, Alaska, June 2015)* pp 299–302
- [12] Zhang Y, Howver R, Gogoi B and Yazdi N 2011 A high-sensitive ultra-thin MEMS capacitive pressure sensor *Proc. Transducers Conf. (Beijing, China, June 2011)* pp 112–5
- [13] Chan C-K, Lai W-C, Wu M, Wang M-Y and Fang W 2011 Design and implementation of a capacitive-type microphone with rigid diaphragm and flexible spring using the two poly silicon micromachining processes *IEEE Sensors J.* **11** 2365–71
- [14] Cheng C-L, Chang H-C, Chang C-I, Tuan Y-T and Fang W 2014 Mechanical force-displacement transduction structure for performance enhancement of CMOS-MEMS pressure sensor *Proc. IEEE MEMS Conf. (San Francisco, CA, January 2014)* pp 757–60
- [15] Yen T-H, Tsai M-H, Chang C-I, Liu Y-C, Li S-S, Chen R, Chiou J-C and Fang W 2011 Improvement of CMOS-MEMS accelerometer using the symmetric layers stacking design *Proc. IEEE Sensors Conf. (Limerick, Ireland, October 2011)* pp 145–8
- [16] Ho S-S, Rajgopal S and Mehregany M 2013 Media compatible stainless steel capacitive pressure sensors *Sensors Actuators A* **189** 134–42
- [17] Lee Y and Wise K 1982 A batch-fabricated silicon capacitive pressure transducer with low temperature sensitivity *IEEE Trans. Electron Devices* **29** 42–8
- [18] Tsai M-H, Sun C-M, Liu Y-C, Wang C and Fang W 2009 Design and application of a metal wet-etching post-process for the improvement of CMOS-MEMS capacitive sensors *J. Micromech. Microeng.* **19** 105017
- [19] Cheng C-L, Tsai M-H and Fang W 2015 Determining the thermal expansion coefficient of thin films for a CMOS MEMS process using test cantilevers *J. Micromech. Microeng.* **25** 025014